26. DARK ENERGY

Revised November 2015 by D. H. Weinberg (OSU) and M. White (UCB, LBL); written November 2013 by M. J. Mortonson (UCB, LBL), D. H. Weinberg (OSU), and M. White (UCB, LBL).

26.1. Repulsive Gravity and Cosmic Acceleration

In the first modern cosmological model, Einstein [1] modified his field equation of General Relativity (GR), introducing a "cosmological term" that enabled a solution with time-independent, spatially homogeneous matter density $\rho_{\rm m}$ and constant positive space curvature. Although Einstein did not frame it this way, one can view the "cosmological constant" Λ as representing a constant energy density of the vacuum [2], whose repulsive gravitational effect balances the attractive gravity of matter and thereby allows a static solution. After the development of dynamic cosmological models [3,4] and the discovery of cosmic expansion [5], the cosmological term appeared unnecessary, and Einstein and de Sitter [6] advocated adopting an expanding, homogeneous and isotropic, spatially flat, matter-dominated universe as the default cosmology until observations dictated otherwise. Such a model has matter density equal to the critical density, $\Omega_{\rm m} \equiv \rho_{\rm m}/\rho_{\rm c} = 1$, and negligible contribution from other energy components [7].

By the mid-1990s, the Einstein-de Sitter model was showing numerous cracks, under the combined onslaught of data from the cosmic microwave background (CMB), large-scale galaxy clustering, and direct estimates of the matter density, the expansion rate (H_0), and the age of the Universe. As noted in a number of papers from this time, introducing a cosmological constant offered a potential resolution of many of these tensions, yielding the most empirically successful version of the inflationary cold dark matter scenario. In the late 1990s, supernova surveys by two independent teams provided direct evidence for accelerating cosmic expansion [8,9], establishing the cosmological constant model (with $\Omega_{\rm m} \approx 0.3$, $\Omega_\Lambda \approx 0.7$) as the preferred alternative to the $\Omega_{\rm m} = 1$ scenario. Shortly thereafter, CMB evidence for a spatially flat universe [10,11], and thus for $\Omega_{\rm tot} \approx 1$, cemented the case for cosmic acceleration by firmly eliminating the free-expansion alternative with $\Omega_{\rm m} \ll 1$ and $\Omega_\Lambda = 0$. Today, the accelerating universe is well established by multiple lines of independent evidence from a tight web of precise cosmological measurements.

As discussed in the Big Bang Cosmology article of this *Review* (Sec. 22), the scale factor $R(t)$ of a homogeneous and isotropic universe governed by GR grows at an accelerating rate if the pressure $p < -\frac{1}{3}\rho$ (in $c = 1$ units). A cosmological constant has $\rho_\Lambda =$ constant and pressure $p_\Lambda = -\rho_\Lambda$ (see Eq. 22.10), so it will drive acceleration if it dominates the total energy density. However, acceleration could arise from a more general form of "dark energy" that has negative pressure, typically specified in terms of the equation-of-state-parameter $w = p/\rho$ ($= -1$ for a cosmological constant). Furthermore, the conclusion that acceleration requires a new energy component beyond matter and radiation relies on the assumption that GR is the correct description of gravity on cosmological scales. The title of this article follows the common but inexact usage of "dark energy" as a catch-all term for the origin of cosmic acceleration, regardless of whether it arises from a new form of energy or a modification of GR. Our account here draws on the much longer review of cosmic acceleration by Ref. [12], which provides

background explanation and extensive literature references for most of the points in this article, but is less up to date in its description of current empirical constraints.

Below we will use the abbreviation ΛCDM to refer to a model with cold dark matter, a cosmological constant, inflationary initial conditions, standard radiation and neutrino content, and a flat universe with $\Omega_{\rm tot} = 1$ (though we will sometimes describe this model as "flat ΛCDM" to emphasize this last restriction). We will use wCDM to denote a model with the same assumptions but a free, constant value of w. Models with the prefix "o" (*e.g.*, owCDM) allow non-zero space curvature.

26.2. Theories of Cosmic Acceleration

26.2.1. *Dark Energy or Modified Gravity?* :

A cosmological constant is the mathematically simplest, and perhaps the physically simplest, theoretical explanation for the accelerating universe. The problem is explaining its unnaturally small magnitude, as discussed in Sec. 22.4.7 of this *Review*. An alternative (which still requires finding a way to make the cosmological constant zero or at least negligibly small) is that the accelerating cosmic expansion is driven by a new form of energy such as a scalar field [13] with potential $V(\phi)$. The energy density and pressure of the field $\phi(\mathbf{x})$ take the same forms as for inflationary scalar fields, given in Eq. (22.52) of the Big Bang Cosmology article. In the limit that $\frac{1}{2}\dot{\phi}^2 \ll |V(\phi)|$, the scalar field acts like a cosmological constant, with $p_\phi \approx -\rho_\phi$. In this scenario, today's cosmic acceleration is closely akin to the epoch of inflation, but with radically different energy and timescale.

More generally, the value of $w = p_\phi/\rho_\phi$ in scalar field models evolves with time in a way that depends on $V(\phi)$ and on the initial conditions $(\phi_i, \dot{\phi}_i)$; some forms of $V(\phi)$ have attractor solutions in which the late-time behavior is insensitive to initial values. Many forms of time evolution are possible, including ones where w is approximately constant and broad classes where w "freezes" towards or "thaws" away from $w = -1$, with the transition occurring when the field comes to dominate the total energy budget. If ρ_ϕ is even approximately constant, then it becomes dynamically insignificant at high redshift, because the matter density scales as $\rho_{\rm m} \propto (1+z)^3$. "Early dark energy" models are ones in which ρ_ϕ is a small but not negligible fraction (*e.g.*, a few percent) of the total energy throughout the matter- and radiation-dominated eras, tracking the dominant component before itself coming to dominate at low redshift.

Instead of introducing a new energy component, one can attempt to modify gravity in a way that leads to accelerated expansion [14]. One option is to replace the Ricci scalar $\mathcal{R}$ with a function $\mathcal{R} + f(\mathcal{R})$ in the gravitational action [15]. Other changes can be more radical, such as introducing extra dimensions and allowing gravitons to "leak" off the brane that represents the observable universe (the "DGP" model [16]) . The DGP example has inspired a more general class of "galileon" and massive gravity models. Constructing viable modified gravity models is challenging, in part because it is easy to introduce theoretical inconsistencies (such as "ghost" fields with negative kinetic energy), but above all because GR is a theory with many high-precision empirical successes on solar system scales [17]. Modified gravity models typically invoke screening mechanisms that force model predictions to approach those of GR in regions of high density or strong

gravitational potential. Screening offers potentially distinctive signatures, as the strength of gravity (*i.e.*, the effective value of $G_{\rm N}$) can vary by order unity in environments with different gravitational potentials.

More generally, one can search for signatures of modified gravity by comparing the history of cosmic structure growth to the history of cosmic expansion. Within GR, these two are linked by a consistency relation, as described below (Eq. (26.2)). Modifying gravity can change the predicted rate of structure growth, and it can make the growth rate dependent on scale or environment. In some circumstances, modifying gravity alters the combinations of potentials responsible for gravitational lensing and the dynamics of non-relativistic tracers (such as galaxies or stars) in different ways (see Sec. 22.4.7 in this *Review*), leading to order unity mismatches between the masses of objects inferred from lensing and those inferred from dynamics in unscreened environments.

At present there are no fully realized and empirically viable modified gravity theories that explain the observed level of cosmic acceleration. The constraints on $f(\mathcal{R})$ models now force them so close to GR that they cannot produce acceleration without introducing a separate dark energy component [18]. The DGP model is empirically ruled out by several tests, including the expansion history, the integrated Sachs-Wolfe effect, and redshift-space distortion measurements of the structure growth rate [19]. The elimination of these models should be considered an important success of the program to empirically test theories of cosmic acceleration. However, it is worth recalling that there was no fully realized gravitational explanation for the precession of Mercury's orbit prior to the completion of GR in 1915, and the fact that no complete and viable modified gravity theory exists today does not mean that one will not arise in the future. In the meantime, we can continue empirical investigations that can tighten restrictions on such theories or perhaps point towards the gravitational sector as the origin of accelerating expansion.

26.2.2. *Expansion History and Growth of Structure* :

The main line of empirical attack on dark energy is to measure the history of cosmic expansion and the history of matter clustering with the greatest achievable precision over a wide range of redshift. Within GR, the expansion rate $H(z)$ is governed by the Friedmann equation (see the articles on Big Bang Cosmology and Cosmological Parameters—Secs. 22 and 24 in this *Review*). For dark energy with an equation of state $w(z)$, the cosmological constant contribution to the expansion, Ω_Λ, is replaced by a redshift-dependent contribution. The evolution of the dark energy density follows from Eq. (22.10),

$$\Omega_{\rm de}\frac{\rho_{\rm de}(z)}{\rho_{\rm de}(z=0)} = \Omega_{\rm de}\exp\left[3\int_0^z [1+w(z')]\frac{dz'}{1+z'}\right] \;=\; \Omega_{\rm de}(1+z)^{3(1+w)}, \qquad (26.1)$$

where the second equality holds for constant w. If $\Omega_{\rm m}$, $\Omega_{\rm r}$, and the present value of $\Omega_{\rm tot}$ are known, then measuring $H(z)$ pins down $w(z)$. (Note that $\Omega_{\rm de}$ is the same quantity denoted $\Omega_{\rm v}$ in Sec. 22, but we have adopted the de subscript to avoid implying that dark energy is necessarily a vacuum effect.)

While some observations can probe $H(z)$ directly, others measure the distance-redshift relation. The basic relations between angular diameter distance or luminosity distance

and $H(z)$ are given in Ch. 22 —and these are generally unaltered in time-dependent dark energy or modified gravity models. For convenience, in later sections, we will sometimes refer to the comoving angular distance, $D_{\rm A,c}(z) = (1+z)D_{\rm A}(z)$.

In GR-based linear perturbation theory, the density contrast $\delta(\mathbf{x},t) \equiv \rho(\mathbf{x},t)/\bar{\rho}(t) - 1$ of pressureless matter grows in proportion to the linear growth function $G(t)$ (not to be confused with the gravitational constant $G_{\rm N}$), which follows the differential equation

$$\ddot{G} + 2H(z)\dot{G} - \frac{3}{2}\Omega_{\rm m}H_0^2(1+z)^3 G = 0\ . \tag{26.2}$$

To a good approximation, the logarithmic derivative of $G(z)$ is

$$f(z) \equiv -\frac{d\ln G}{d\ln(1+z)} \approx \left[\Omega_{\rm m}(1+z)^3\frac{H_0^2}{H^2(z)}\right]^{\gamma}\ , \tag{26.3}$$

where $\gamma \approx 0.55$ for relevant values of cosmological parameters [20]. In an $\Omega_{\rm m} = 1$ universe, $G(z) \propto (1+z)^{-1}$, but growth slows when $\Omega_{\rm m}$ drops significantly below unity. One can integrate Eq. (26.3) to get an approximate integral relation between $G(z)$ and $H(z)$, but the full (numerical) solution to Eq. (26.2) should be used for precision calculations. Even in the non-linear regime, the amplitude of clustering is determined mainly by $G(z)$, so observations of non-linear structure can be used to infer the linear $G(z)$, provided one has good theoretical modeling to relate the two.

In modified gravity models the growth rate of gravitational clustering may differ from the GR prediction. A general strategy to test modified gravity, therefore, is to measure both the expansion history and the growth history to see whether they yield consistent results for $H(z)$ or $w(z)$.

26.2.3. *Parameters* :

Constraining a general history of $w(z)$ is nearly impossible, because the dark energy density, which affects $H(z)$, is given by an integral over $w(z)$, and distances and the growth factor involve a further integration over functions of $H(z)$. Oscillations in $w(z)$ over a range $\Delta z/(1+z) \ll 1$ are therefore extremely difficult to constrain. It has become conventional to phrase constraints or projected constraints on $w(z)$ in terms of a linear evolution model,

$$w(a) = w_0 + w_a(1-a) = w_{\rm p} + w_a(a_{\rm p} - a), \tag{26.4}$$

where $a \equiv (1+z)^{-1}$, w_0 is the value of w at $z = 0$, and $w_{\rm p}$ is the value of w at a "pivot" redshift $z_{\rm p} \equiv a_{\rm p}^{-1} - 1$, where it is best constrained by a given set of experiments. For typical data combinations, $z_{\rm p} \approx 0.5$. This simple parameterization can provide a good approximation to the predictions of many physically motivated models for observables measured with percent-level precision. A widely used "Figure of Merit" (FoM) for dark energy experiments [21] is the projected combination of errors $[\sigma(w_{\rm p})\sigma(w_a)]^{-1}$. Ambitious future experiments with 0.1–0.3% precision on observables can constrain richer descriptions of $w(z)$, which can be characterized by principal components.

There has been less convergence on a standard parameterization for describing modified gravity theories. Deviations from the GR-predicted growth rate can be described by

a deviation $\Delta\gamma$ in the index of Eq. (26.3), together with an overall multiplicative offset relative to the $G(z)$ expected from extrapolating the CMB-measured fluctuation amplitude to low redshift. However, these two parameters may not accurately capture the growth predictions of all physically interesting models. Another important parameter to constrain is the ratio of the gravitational potentials governing space curvature and the acceleration of non-relativistic test particles. The possible phenomenology of modified gravity models is rich, which enables many consistency tests but complicates the task of constructing parameterized descriptions.

The more general set of cosmological parameters is discussed elsewhere in this *Review* (Sec. 24), but here we highlight a few that are particularly important to the dark energy discussion:

- The dimensionless Hubble parameter $h \equiv H_0/100\,\mathrm{km\,s^{-1}\,Mpc^{-1}}$ determines the present day value of the critical density and the overall scaling of distances inferred from redshifts.
- Ω_m and Ω_tot affect the expansion history and the distance-redshift relation.
- The sound horizon $r_\mathrm{s} = \int_0^{t_\mathrm{rec}} c_\mathrm{s}(t)dt/a(t)$, the comoving distance that pressure waves can propagate between $t = 0$ and recombination, determines the physical scale of the acoustic peaks in the CMB and the baryon acoustic oscillation (BAO) feature in low redshift matter clustering [22].
- The amplitude of matter fluctuations, conventionally represented by the quantity $\sigma_8(z)$, scales the overall amplitude of growth measures such as weak lensing or redshift-space distortions (discussed in the next section).

Specifically, $\sigma_8(z)$ refers to the rms fluctuation of the matter overdensity $\rho/\bar{\rho}$ in spheres of radius $8\,h^{-1}$Mpc, computed from the linear theory matter power spectrum at redshift z, and σ_8 on its own refers to the value at $z = 0$ (just like our convention for Ω_m).

While discussions of dark energy are frequently phrased in terms of values and errors on quantities like w_p, w_a, $\Delta\gamma$, and Ω_tot, parameter precision is the means to an end, not an end in itself. The underlying goal of empirical studies of cosmic acceleration is to address two physically profound questions:

1. Does acceleration arise from a breakdown of GR on cosmological scales or from a new energy component that exerts repulsive gravity within GR?
2. If acceleration is caused by a new energy component, is its energy density constant in space and time, as expected for a fundamental vacuum energy, or does it show variations that indicate a dynamical field?

Substantial progress towards answering these questions, in particular any definitive rejection of the cosmological constant "null hypothesis," would be a major breakthrough in cosmology and fundamental physics.

26.3. Observational Probes

We briefly summarize the observational probes that play the greatest role in current constraints on dark energy. Further discussion can be found in other articles of this *Review*, in particular Secs. 24 (Cosmological Parameters) and 27 (The Cosmic Microwave Background), and in Ref. [12], which provides extensive references to background literature. Recent observational results from these methods are discussed in 26.4.

26.3.1. *Methods, Sensitivity, Systematics* :

Cosmic Microwave Background Anisotropies: Although CMB anisotropies provide limited information about dark energy on their own, CMB constraints on the geometry, matter content, and radiation content of the Universe play a critical role in dark energy studies when combined with low redshift probes. In particular, CMB data supply measurements of $\theta_{\rm s} = r_{\rm s}/D_{\rm A,c}(z_{\rm rec})$, the angular size of the sound horizon at recombination, from the angular location of the acoustic peaks, measurements of $\Omega_{\rm m}h^2$ and $\Omega_{\rm b}h^2$ from the heights of the peaks, and normalization of the amplitude of matter fluctuations at $z_{\rm rec}$ from the amplitude of the CMB fluctuations themselves. *Planck* data yield a 0.4% determination of r_s, which scales as $(\Omega_{\rm m}h^2)^{-0.25}$ for cosmologies with standard matter and radiation content. The uncertainty in the matter fluctuation amplitude is $1-2\%$. Improvements in the measurement of the electron scattering optical depth τ, with future analyses of *Planck* polarization maps, would reduce this uncertainty further. Secondary anisotropies, including the Integrated Sachs-Wolfe effect and the Sunyaev-Zeldovich (SZ, [23]) effect, provide additional information about dark energy by constraining low-redshift structure growth.

Type Ia Supernovae: Type Ia supernovae, produced by the thermonuclear explosions of white dwarfs, exhibit $10-15\%$ scatter in peak luminosity after correction for light curve duration (the time to rise and fall) and color (which is a diagnostic of dust extinction). Since the peak luminosity is not known *a priori*, supernova surveys constrain ratios of luminosity distances at different redshifts. If one is comparing a high redshift sample to a local calibrator sample measured with much higher precision (and distances inferred from Hubble's law), then one essentially measures the luminosity distance in h^{-1}Mpc, constraining the combination $hD_{\rm L}(z)$. With distance uncertainties of 5–8% per well observed supernova, a sample of around 100 SNe is sufficient to achieve sub-percent statistical precision. The 1–2% systematic uncertainties in current samples are dominated by uncertainties associated with photometric calibration and dust extinction corrections plus the observed dependence of luminosity on host galaxy properties. Another potential systematic is redshift evolution of the supernova population itself, which can be tested by analyzing subsamples grouped by spectral properties or host galaxy properties to confirm that they yield consistent results.

Baryon Acoustic Oscillations (BAO): Pressure waves that propagate in the pre-recombination photon-baryon fluid imprint a characteristic scale in the clustering of matter and galaxies, which appears in the galaxy correlation function as a localized peak at the sound horizon scale $r_{\rm s}$, or in the power spectrum as a series of oscillations. Since observed galaxy coordinates consist of angles and redshifts, measuring this "standard ruler" scale in a galaxy redshift survey determines the angular diameter distance

$D_{\rm A}(z)$ and the expansion rate $H(z)$, which convert coordinate separations to comoving distances. Errors on the two quantities are correlated, and in existing galaxy surveys the best determined combination is approximately $D_{\rm V}(z) = [czD^2_{\rm A,c}(z)/H(z)]^{1/3}$. As an approximate rule of thumb, a survey that fully samples structures at redshift z over a comoving volume V, and is therefore limited by cosmic variance rather than shot noise, measures $D_{\rm A,c}(z)$ with a fractional error of $0.005(V/10\,{\rm Gpc}^3)^{-1/2}$ and $H(z)$ with a fractional error $1.6-1.8$ times higher. The most precise BAO measurements to date come from large galaxy redshift surveys probing $z<0.8$, and these will be extended to higher redshifts by future projects. At redshifts $z>2$, BAO can also be measured in the Lyman-α forest of intergalactic hydrogen absorption towards background quasars, where the fluctuating absorption pattern provides tens or hundreds of samples of the density field along each quasar sightline. For Lyman-α forest BAO, the best measured parameter combination is more heavily weighted towards $H(z)$ because of strong redshift-space distortions that enhance clustering in the line-of-sight direction. Radio intensity mapping, which maps large scale structure in redshifted 21cm hydrogen emission without resolving individual galaxies, offers a potentially promising route to measuring BAO over large volumes at relatively low cost, but the technique is still under development. Photometric redshifts in optical imaging surveys can be used to measure BAO in the angular direction, though the typical distance precision is a factor of $3-4$ lower compared to a well sampled spectroscopic survey of the same area, and angular BAO measurements do not directly constrain $H(z)$. BAO distance measurements complement SN distance measurements by providing absolute rather than relative distances (with precise calibration of $r_{\rm s}$ from the CMB) and by having greater achievable precision at high redshift thanks to the increasing comoving volume available. Theoretical modeling suggests that BAO measurements from even the largest feasible redshift surveys will be limited by statistical rather than systematic uncertainties.

Weak Gravitational Lensing: Gravitational light bending by a clustered distribution of matter shears the shapes of higher redshift background galaxies in a spatially coherent manner, producing a correlated pattern of apparent ellipticities. By studying the weak lensing signal for source galaxies binned by photometric redshift (estimated from broad-band colors), one can probe the history of structure growth. For a specified expansion history, the predicted signal scales approximately as $\sigma_8\Omega_{\rm m}^{\alpha}$, with $\alpha\approx 0.3$–0.5. The predicted signal also depends on the distance-redshift relation, so weak lensing becomes more powerful in concert with SN or BAO measurements that can pin this relation down independently. The most challenging systematics are shape measurement biases, biases in the distribution of photometric redshifts, and intrinsic alignments of galaxy orientations that could contaminate the lensing-induced signal. Predicting the large-scale weak lensing signal is straightforward in principle, but the number of independent modes on large scales is small, and the inferences are therefore dominated by sample variance. Exploiting small-scale measurements, for tighter constraints, requires modeling the effects of complex physical processes such as star formation and feedback on the matter power spectrum. Strong gravitational lensing can also provide constraints on dark energy, either through time delay measurements that probe the absolute distance scale, or through measurements of multiple-redshift lenses that constrain distance ratios.

The primary uncertainty for strong lensing constraints is modeling the mass distribution of the lens systems.

Clusters of Galaxies: Like weak lensing, the abundance of massive dark matter halos probes structure growth by constraining $\sigma_8\Omega_{\rm m}^{\alpha}$, where $\alpha \approx 0.3$–0.5. These halos can be identified as dense concentrations of galaxies or through the signatures of hot (10^7–10^8 K) gas in X-ray emission or SZ distortion of the CMB. The critical challenge in cluster cosmology is calibrating the relation $P(M_{\rm halo}|O)$ between the halo mass as predicted from theory and the observable O used for cluster identification. Measuring the stacked weak lensing signal from clusters has emerged as a promising approach to achieve percent-level accuracy in calibration of the mean relation, which is required for clusters to remain competitive with other growth probes. This method requires accurate modeling of completeness and contamination of cluster catalogs, projection effects on cluster selection and weak lensing measurements, and possible baryonic physics effects on the mass distribution within clusters.

Redshift-Space Distortions (RSD) and the Alcock-Paczynksi (AP) Effect: Redshift-space distortions of galaxy clustering, induced by peculiar motions, probe structure growth by constraining the parameter combination $f(z)\sigma_8(z)$, where $f(z)$ is the growth rate defined by Eq. (26.3). Uncertainties in theoretical modeling of non-linear gravitational evolution and the non-linear bias between the galaxy and matter distributions currently limit application of the method to large scales (comoving separations $r \gtrsim 10\,h^{-1}$Mpc or wavenumbers $k \lesssim 0.2h\,{\rm Mpc}^{-1}$). A second source of anisotropy arises if one adopts the wrong cosmological metric to convert angles and redshifts into comoving separations, a phenomenon known as the Alcock-Paczynksi effect [24]. Demanding isotropy of clustering at redshift z constrains the parameter combination $H(z)D_{\rm A}(z)$. The main challenge for the AP method is correcting for the anisotropy induced by peculiar velocity RSD.

Direct Determination of H_0: The value of H_0 sets the current value of the critical density $\rho_{\rm c} = 3H_0^2/8\pi G_{\rm N}$, and combination with CMB measurements provides a long lever arm for constraining the evolution of dark energy. The challenge in direct H_0 measurements is establishing distances to galaxies that are "in the Hubble flow," *i.e.*, far enough away that their peculiar velocities are small compared to the expansion velocity $v = H_0 d$. This can be done by building a ladder of distance indicators tied to stellar parallax on its lowest rung, or by using gravitational lens time delays or geometrical measurements of maser data to circumvent this ladder.

26.3.2. *Dark Energy Experiments* :

Most observational applications of these methods now take place in the context of large cosmological surveys, for which constraining dark energy and modified gravity theories is a central objective. Table 26.1 lists a selection of current and planned dark energy experiments, taken from the Snowmass 2013 Dark Energy Facilities review [25], which focused on projects in which the U.S. has either a leading role or significant participation. References and links to further information about these projects can be found in Ref. [25].

Table 26.1: A selection of major dark energy experiments, based on Ref. [25]. Abbreviations in the "Data" column refer to optical (Opt) or near-infrared (NIR) imaging (I) or spectroscopy (S). For spectroscopic experiments, the "Spec-z" column lists the primary redshift range for galaxies (gals), quasars (QSOs), or the Lyman-α forest (LyαF). Abbreviations in the "Methods" column are weak lensing (WL), clusters (CL), supernovae (SN), baryon acoustic oscillations (BAO), and redshift-space distortions (RSD).

Project	Dates	Area/deg^2	Data	Spec-z Range	Methods
BOSS	2008-2014	10,000	Opt-S	$0.3-0.7$ (gals)	BAO/RSD
				$2-3.5$ (LyαF)	
DES	2013-2018	5000	Opt-I	——	WL/CL
					SN/BAO
eBOSS	2014-2020	7500	Opt-S	$0.6-2.0$ (gal/QSO)	BAO/RSD
				$2-3.5$ (LyαF)	
SuMIRE	2014-2024	1500	Opt-I		WL/CL
			Opt/NIR-S	$0.8-2.4$ (gals)	BAO/RSD
HETDEX	2014-2019	300	Opt-S	$1.9 < z < 3.5$ (gals)	BAO/RSD
DESI	2019-2024	14,000	Opt-S	$0-1.7$ (gals)	BAO/RSD
				$2-3.5$ (LyαF)	
LSST	2020-2030	20,000	Opt-I	——	WL/CL
					SN/BAO
Euclid	2020-2026	15,000	Opt-I		WL/CL
			NIR-S	$0.7-2.2$ (gals)	BAO/RSD
WFIRST	2024-2030	2200	NIR-I		WL/CL/SN
			NIR-S	$1.0-3.0$ (gals)	BAO/RSD

Beginning our discussion with imaging surveys, the Dark Energy Survey (DES) will cover 1/8 of the sky to a depth roughly 2 magnitudes deeper than the Sloan Digital Sky Survey (SDSS), enabling weak lensing measurements with unprecedented statistical precision, cluster measurements calibrated by weak lensing, and angular BAO measurements based on photometric redshifts. With repeat imaging over a smaller area, DES will identify thousands of Type Ia SNe, which together with spectroscopic follow-up data will enable significant improvements on the current state-of-the-art for supernova (SN) cosmology. The Hyper-Suprime Camera (HSC) on the Subaru 8.2-meter telescope will carry out a similar type of optical imaging survey, probing a smaller area than DES but to greater depth. This survey is one component of the Subaru Measurement of Images and Redshifts (SuMIRE) project. Beginning in the early 2020s, the dedicated Large Synoptic Survey Telescope (LSST) will scan the southern sky to SDSS-like depth

every four nights. LSST imaging co-added over its decade-long primary survey will reach extraordinary depth, enabling weak lensing, cluster, and photometric BAO studies from billions of galaxies. LSST time-domain monitoring will identify and measure light curves for thousands of Type Ia SNe per year.

Turning to spectroscopic surveys, the Baryon Oscillation Spectroscopic Survey (BOSS) and its successor eBOSS use fiber-fed optical spectrographs to map the redshift-space distributions of millions of galaxies and quasars. These 3-dimensional maps enable BAO and RSD measurements, and Lyman-α forest spectra of high-redshift quasars extend these measurements to redshifts $z > 2$. The Hobby-Eberly Telescope Dark Energy Experiment (HETDEX) uses integral field spectrographs to detect Lyman-α emission-line galaxies at $z \approx 1.9 - 3.5$, probing a small sky area but a substantial comoving volume. The Dark Energy Spectroscopic Instument (DESI) follows a strategy similar to BOSS/eBOSS but on a much grander scale, using a larger telescope (4-meter vs. 2.5-meter) and a much higher fiber multiplex (5000 vs. 1000) to survey an order-of-magnitude more galaxies. A new Prime Focus Spectrograph (PFS) for the Subaru telescope will enable the spectroscopic component of SuMIRE, with the large telescope aperture and wavelength sensitivity that extends to the near-infrared (NIR) allowing it to probe a higher redshift galaxy population than DESI, over a smaller area of sky.

Compared to ground-based observations, space observations afford higher angular resolution and a far lower NIR sky background. The *Euclid* and *WFIRST* (*Wide Field Infrared Survey Telescope*) missions will exploit these advantages, conducting large area imaging surveys for weak lensing and cluster studies and slitless spectroscopic surveys of emission-line galaxies for BAO and RSD studies. *WFIRST* also incorporates an imaging and spectrophotometric supernova (SN) survey, extending to redshift $z \approx 1.7$. Survey details are likely to evolve prior to launch, but in the current designs one can roughly characterize the difference between the *Euclid* and *WFIRST* dark energy experiments as "wide vs. deep," with planned survey areas of 15,000 deg^2 and 2200 deg^2, respectively. For weak lensing shape measurements, *Euclid* uses a single wide optical filter, while *WFIRST* uses three NIR filters. The *Euclid* galaxy redshift survey covers a large volume at relatively low space density, while the *WFIRST* survey provides denser sampling of structure in a smaller volume. There are numerous synergies among the LSST, *Euclid*, and *WFIRST* dark energy programs, as discussed in Ref. [26].

26.4. Current Constraints on Expansion, Growth, and Dark Energy

The last decade has seen dramatic progress in measurements of the cosmic expansion history and structure growth, leading to much tighter constraints on the parameters of dark energy models. CMB data from the *WMAP* and *Planck* satellites and from higher resolution ground-based experiments have provided an exquisitely detailed picture of structure at the recombination epoch and the first CMB-based measures of low redshift structure through lensing and SZ cluster counts. Cosmological supernova samples have increased in size from tens to many hundreds, with continuous coverage from $z = 0$ to $z \approx 1.4$, alongside major improvements in data quality, analysis methods,

and detailed understanding of local populations. BAO measurements have advanced from the first detections to $1-2\%$ precision at multiple redshifts, with increasingly sophisticated methods for testing systematics, fitting models, and evaluating statistical errors. Constraints on low redshift structure from galaxy clusters have become more robust, with improved X-ray and SZ data and weak lensing mass calibrations, and they have been joined by the first precise structure constraints from cosmic shear weak lensing, galaxy-galaxy lensing, and redshift-space distortions. The precision of direct H_0 measurements has sharpened from the roughly 10% error of the *HST* Key Project [27] to 3–4% in some recent analyses.

Our summary of current constraints here relies heavily on the analysis of Ref. [28], who combine BAO measurements, SN measurements, and *Planck* CMB data to examine a variety of dark energy models. While Ref. [28] uses the 2013 *Planck* data [29] rather than the 2015 data [30], we expect that changing to the 2015 data would make negligible difference to best-fit parameter values and only small changes to the statistical uncertainties on combined CMB+BAO+SN constraints. An analysis of dark energy and modified gravity models by the *Planck* team, using the 2015 *Planck* data and a somewhat different selection of low redshift data and model parameterizations, can be found in Ref. [31].

As an illustration of current measurements of the cosmic expansion history, Fig. 26.1 compares distance-redshift measurements from SN and BAO data to the predictions for a flat universe with a cosmological constant. SN cosmology relies on compilation analyses that try to bring data from different surveys probing distinct redshift ranges to a common scale. Here we use the "joint light curve analysis" (JLA) sample of Ref. [33], who carried out a careful intercalibration of the 3-year Supernova Legacy Survey (SNLS3, [34]) and the full SDSS-II Supernova Survey [35] data in combination with several local supernova samples and high-redshift supernovae from *HST*. Results from the Union2.1 sample [36], which partly overlaps JLA but has different analysis procedures, would be similar. For illustration purposes, we have binned the JLA data in redshift and plotted the diagonal elements of the covariance matrix as error bars, and we have converted the SN luminosity distances to an equivalent comoving angular diameter distance. Because the peak luminosity of a fiducial SN Ia is an unknown free parameter, the SN distance measurements could all be shifted up and down by a constant multiplicative factor; cosmological information resides in the relative distances as a function of redshift. For BAO data points we use the compilation of Ref. [28], taken from BAO analyses of the 6dFGS survey [37], the SDSS-II Main Galaxy Sample [38], and the LOWZ and CMASS galaxy samples of BOSS [39]. For the first three data points, values of $D_{\rm V}$ have been converted to $D_{\rm A,c}$, while the CMASS data point uses the angular diameter distance measured directly from anisotropic BAO analysis. The BAO measurements are converted to absolute distances using the sound horizon scale $r_{\rm s} = 147.49$ Mpc from *Planck* 2013 CMB data, whose 0.4% uncertainty is small compared to the current BAO measurement errors.

The plotted cosmological model has $\Omega_{\rm m} = 0.308$ and $h = 0.678$, the best-fit values from *Planck* (TT+lowP+lensing) assuming $w = -1$ and $\Omega_{\rm tot} = 1$ [32]. The SN, BAO, and CMB data sets, probing a wide range of redshifts with radically different techniques, are

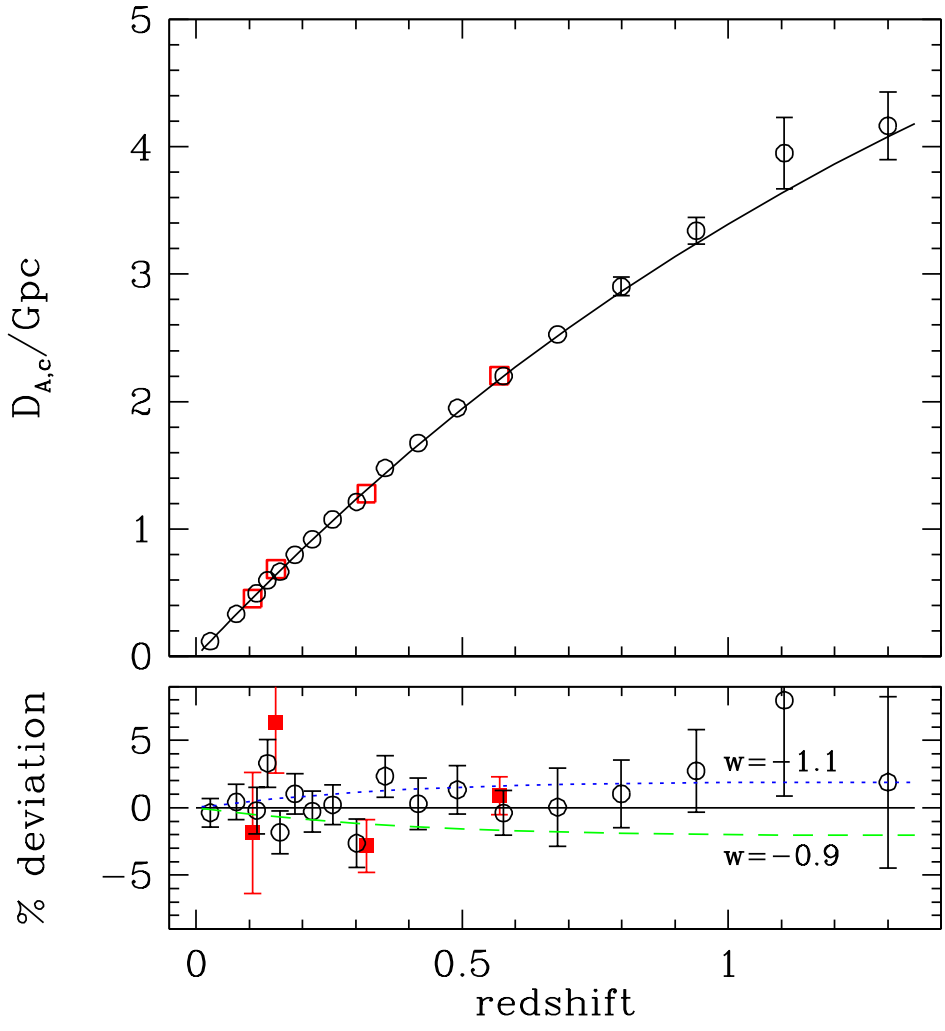

Figure 26.1: The distance-redshift relation measured from Type Ia SNe and BAO compared to the predictions (black curve) of a flat ΛCDM model with $\Omega_{\rm m} = 0.308$ and $h = 0.678$, the best-fit parameters inferred from *Planck* CMB data [32]. Circles show binned luminosity distances from the JLA SN sample [33], multiplied by $(1+z)^{-1}$ to convert to comoving angular diameter distance. Squares show BAO distance measurements, converted to $D_{\rm A,c}(z)$ for the *Planck* cosmology and sound horizon, taken from Ref. [28]. The lower panel plots residuals from the ΛCDM prediction, with dashed and dotted curves that show the effect of changing w by ± 0.1 while all other parameters are held fixed. Note that the SN data points can be shifted up or down by a constant factor to account for freedom in the peak luminosity, while the BAO points are calibrated to 0.4% precision by the sound horizon scale computed from *Planck* data. In the upper panel, error bars are plotted only at $z > 0.7$ to avoid visual confusion.

mutually consistent with the predictions of a flat ΛCDM cosmology. Other curves in the

lower panel of Fig. 26.1 show the effect of changing w by ± 0.1 with all other parameters held fixed. However, such a single-parameter comparison does not capture the impact of parameter degeneracies or the ability of complementary data sets to break them, and if one instead forced a match to CMB data by changing h and $\Omega_{\rm m}$ when changing w then the predicted BAO distances would diverge at $z = 0$ rather than converging there.

Figure 26.2, taken directly from [28], shows cosmological parameter constraints in a series of models with increasingly flexible assumptions (from top left to bottom right) about dark energy and space curvature. These constraints use the BAO distance measurements shown in Fig.26.1, with the separate $D_{\rm A,c}(z)$ and $H(z)$ constraints from the BOSS CMASS sample at $z = 0.57$. They also include BAO constraints on $D_{\rm A,c}(z)$ and $H(z)$ at $z = 2.34$ from the BOSS Lyman-α forest as reported by Ref. [40]. They adopt the JLA SN data set plotted in Fig. 26.1, taking into account the full error covariance matrix reported by Ref. [33], which includes a detailed estimate of systematic uncertainties. The *Planck* CMB data are compressed into constraints on the baryon density $\Omega_{\rm b}h^2$, the sum of baryon and CDM densities $\Omega_{\rm m}h^2$, and the ratio $D_{\rm A,c}(1090)/r_{\rm s}$ of the comoving angular diameter distance to redshift $z = 1090$ divided by the sound horizon. Best-fit values and the 3×3 covariance matrix of these quantities are determined from the public *Planck* likelihood chains. For the data combinations and models shown here, this compressed description captures the information content of the full CMB power spectrum almost perfectly; this would no longer be true when considering models with non-minimal neutrino mass or data sets that constrain the amplitude of matter clustering. Constraints from the full data combination on selected cosmological parameters for three dark energy models are listed in Table 26.2; this is a small subset of the models and data combinations reported in table IV of Ref. [28].

Table 26.2: Constraints on parameters (68% confidence limits) from the combination of BAO, SN, and CMB data as reported by Ref. [28], for three choices of model assumptions: constant w with a flat universe, constant w with free space curvature, and evolving w with a flat universe. In the third model, the constraint on w is reported at $z = 0.266$, where it is best constrained.

	Model		
Parameter	wCDM (flat)	owCDM	w_0w_aCDM (flat)
w	-0.97 ± 0.05	-0.98 ± 0.06	-0.97 ± 0.05
w_a	0 (assumed)	0 (assumed)	-0.2 ± 0.4
$\Omega_{\rm m}$	0.305 ± 0.010	0.303 ± 0.010	0.307 ± 0.011
$\Omega_{\rm tot}$	1.0 (assumed)	1.002 ± 0.003	1.0 (assumed)
h	0.676 ± 0.011	0.676 ± 0.011	0.676 ± 0.011
$\sigma_8(\Omega_{\rm m}/0.30)^{0.4}$	0.811 ± 0.021	0.805 ± 0.022	0.821 ± 0.030

There are numerous points to take away from Fig. 26.2 and Table 26.2. For the

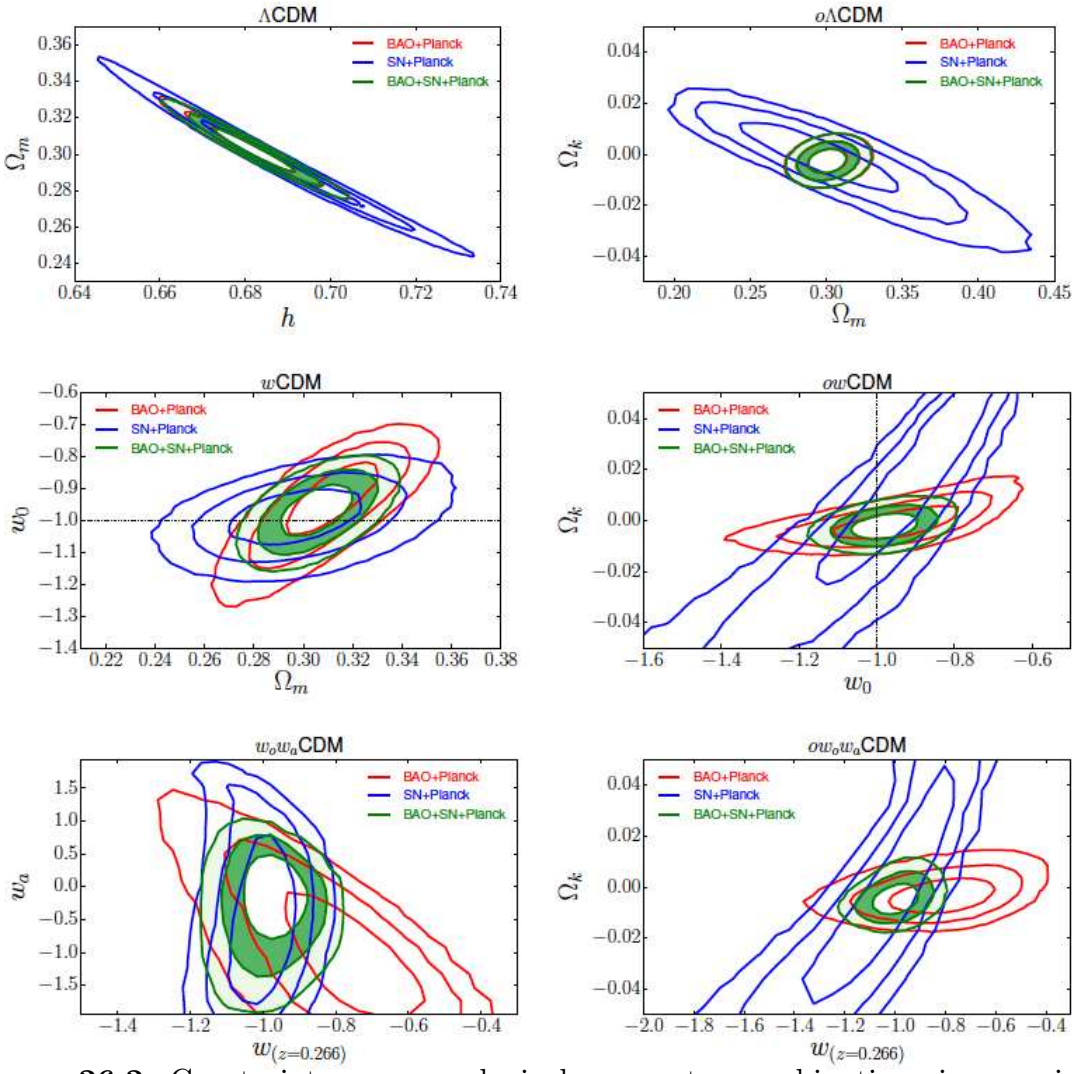

Figure 26.2: Constraints on cosmological parameter combinations in a variety of dark energy models, taken from Ref. [28]. In each panel: red curves show 68%, 95%, and 99.7% confidence contours from BAO measurements with *Planck* CMB constraints; blue contours show the combination of SN measurements with *Planck* CMB; and green contours show the combination of all three, with the white zone interior to the dark green annulus marking the 68% confidence region. The upper left panel shows $(\Omega_{\rm m}, h)$ constraints assuming a flat universe with a cosmological constant. The upper right panel shows $(\Omega_{\rm m}, \Omega_K)$ constraints assuming a cosmological constant but allowing non-zero space curvature. The middle row shows constraints with the dark energy equation-of-state w_0 as a (constant) free parameter, assuming a flat universe on the left and allowing non-zero curvature on the right. The bottom row shows the corresponding constraints for models with an evolving equation-of-state parameter $w(a) = w_0 + w_a(1-a)$. In the bottom panels the x-axis quantity is the value of w at $z = 0.266$, the redshift at which it is best constrained by the full data combination in the flat universe model.

flat ΛCDM model, the combination of CMB and BAO data provides tight constraints on parameters, as discussed at greater length in Sec. 24 of this *Review*. Assuming a cosmological constant, the CMB+BAO combination yields a tight constraint on space curvature consistent with a flat universe, implying $\Omega_{\rm tot} = 1.002 \pm 0.003$. The addition of SN data does not tighten the constraints in cosmological constant models (top row), but it significantly tightens constraints in models that allow an evolving dark energy density. In all of the more flexible models, the parameter values of flat ΛCDM ($w = -1$, $w_a = 0$, $\Omega_K = 0$) lie within the 68% confidence region of the full CMB+BAO+SN combination. Even with the flexibility of an evolving equation of state governed by Eq. (26.4), curvature is tightly constrained by the full data combination. For a constant equation of state, the error on w is ≈ 0.05, and even in the $w_0 - w_a$ model the value of w at the pivot redshift $z_p = 0.266$ is constrained to ± 0.05. However, the full CMB+BAO+SN data combination still provides only weak constraints on evolution of the equation of state, allowing $w_a = -0.2 \pm 0.4$ even when assuming a flat universe.

As discussed by [28], the flat ΛCDM model provides a statistically good fit to the CMB+BAO+SN data combination presented here. However, the Lyman-α forest BAO measurements at $z \approx 2.3$ disagree with the model predictions at the $\approx 2.5\sigma$ level [40]. None of the more flexible models illustrated in Fig. 26.2 significantly reduces this tension, and Ref. [28] considers a variety of more elaborate models (decaying dark matter, early dark energy, massive neutrinos, additional relativistic species) that also fail to remove it. The lack of a plausible alternative model, and the acceptable total χ^2 when all data points are considered equally, suggests that the discrepancy with Lyman-α forest BAO is either a statistical fluke or an unrecognized systematic bias in the measurement. This remains an interesting area for future investigation, as a tightening of error bars without a change in central value would imply a breakdown of this entire class of dark energy models at $z \approx 2 - 3$, or an unanticipated astrophysical effect on the imprint of BAO in the Lyman-α forest.

The 2014 edition of this review highlighted two areas of tension between predictions of the flat ΛCDM model and low-redshift observations: distance-ladder measurements of H_0 and weak lensing or cluster estimates of matter fluctuations. A ΛCDM fit to *Planck* data alone predicts $H_0 = 67.8 \pm 0.9\,{\rm km\,s^{-1}\,Mpc^{-1}}$ (see Chapter 27 of this *Review*). This is lower than most recent determinations of H_0 that use *HST* observations of Cepheid variables in external galaxies to calibrate secondary distance indicators, particularly Type Ia SNe, which can in turn measure distances to galaxies in the Hubble flow. For example, Ref. [41] finds $H_0 = 73.8 \pm 2.4\,{\rm km\,s^{-1}\,Mpc^{-1}}$ and Ref. [42] finds $H_0 = 74.3 \pm 2.1\,{\rm km\,s^{-1}\,Mpc^{-1}}$, with both groups including an estimate of systematic uncertainties in their error budgets. However, Ref. [43], reanalyzing the data set of Ref. [41] with a different treatment of outliers, argues for a lower central value and larger error bars, which together reduce the tension with *Planck*+ΛCDM below 2σ significance. More recently, Ref. [44] have argued that correcting the Ref. [41] value for an offset of SNIa luminosities between star-forming and passive environments lowers the inferred H_0 to $70.6 \pm 2.6\,{\rm km\,s^{-1}\,Mpc^{-1}}$, consistent with the CMB at the 1σ level.

Another recent development is the "inverse distance ladder" determination of H_0 by Ref. [28], who combine the BAO and SN data shown in Fig. 26.1 with the

Planck-calibrated value of the sound horizon scale, $r_s = 147.49 \pm 0.59$ Mpc. The CMB-only prediction of H_0 depends critically on the assumptions of a flat universe and a cosmological constant, and loosening either assumption allows a much wider range of H_0. The method of Ref. [28], by contrast, is insensitive to assumptions about flatness or dark energy, because BAO provide precise absolute distance measurements at $z = 0.3 - 0.6$, and the high-precision relative distance scale from SNe transfers this absolute measurement to $z = 0$, using empirical data instead of an adopted cosmological model. Even allowing a very flexible dark energy parameterization and non-zero space curvature, Ref. [28] obtains 1.7% precision on H_0, with a value $H_0 = 67.3 \pm 1.1\,\mathrm{km\,s^{-1}\,Mpc^{-1}}$ in essentially perfect agreement with the *Planck*+ΛCDM prediction. These measurements could still be reconciled with $H_0 \geq 70\,\mathrm{km\,s^{-1}\,Mpc^{-1}}$ by altering the *pre-recombination* physics of the standard model in a way that shrinks the BAO standard ruler, for instance by adding extra relativistic degrees of freedom. However, it seems increasingly unlikely that the Cepheid-based measurements of H_0 are telling us something surprising about the late time behavior of dark energy, and more likely that they simply overestimate the true value.

The amplitude of CMB anisotropies is proportional to the amplitude of density fluctuations present at recombination, and by assuming GR and a specified dark energy model one can extrapolate the growth of structure forward to the present day to predict σ_8. As discussed in Sec. 26.3, probes of low redshift structure typically constrain the combination $\sigma_8 \Omega_m^\alpha$ with $\alpha \approx 0.3$–0.5. Figure 26.3, taken from Ref. [28], compares predictions of low redshift clustering (black points) from models constrained by CMB+BAO+SN to a variety of observational estimates (red points). The model assumed for each prediction is indicated on the left axis. In the left panel, estimates of $\sigma_8(\Omega_m/0.30)^{0.4}$ at $z \approx 0$ come from cosmic shear (points labeled Hey13, Jee13 in Fig. 26.3), from galaxy-galaxy lensing (Man13), and from clusters (Vik09, Roz10, Pla13, Man14; see Ref. [28] for the observational references). In the middle panel, the values of $\sigma_8(z = 0.57) f(z = 0.57)$ come from three RSD analyses of the BOSS galaxy survey; these analyses use different modeling methods but examine largely the same data. In the right panel the estimate of $\sigma_8(z = 2.5)$ comes from modeling the 1-dimensional power spectrum of the BOSS Lyman-α forest. In the left panel, many but not all of the estimates lie below the model predictions. A straight unweighted average of the observational data points yields $\sigma_8(\Omega_m/0.3)^{0.4} = 0.766 \pm 0.012$, while the flat ΛCDM prediction is 0.821 ± 0.018. This difference is $\approx 2\sigma$, but the key question is whether some of the estimates are systematically biased, and if so which ones. In the middle panel, the RSD growth estimates again lie below the model predictions, but the observational uncertainties are too large to draw an interesting conclusion. At $z = 2.5$, on the other hand, the fluctuation amplitude inferred from the Lyman-α forest is (slightly) above the model prediction.

Relative to our 2014 *Review* (which compared ΛCDM to the constraints labeled here as Hey13, Vik09, Roz10, and Pla13), the addition of new data has made the case for a conflict in matter clustering weaker, or at least more confused. The 2015 *Planck* data add two further ingredients to this discussion. First, they confirm the high normalization of (σ_8, Ω_m) relative to earlier values from *WMAP*, indicating that the high model

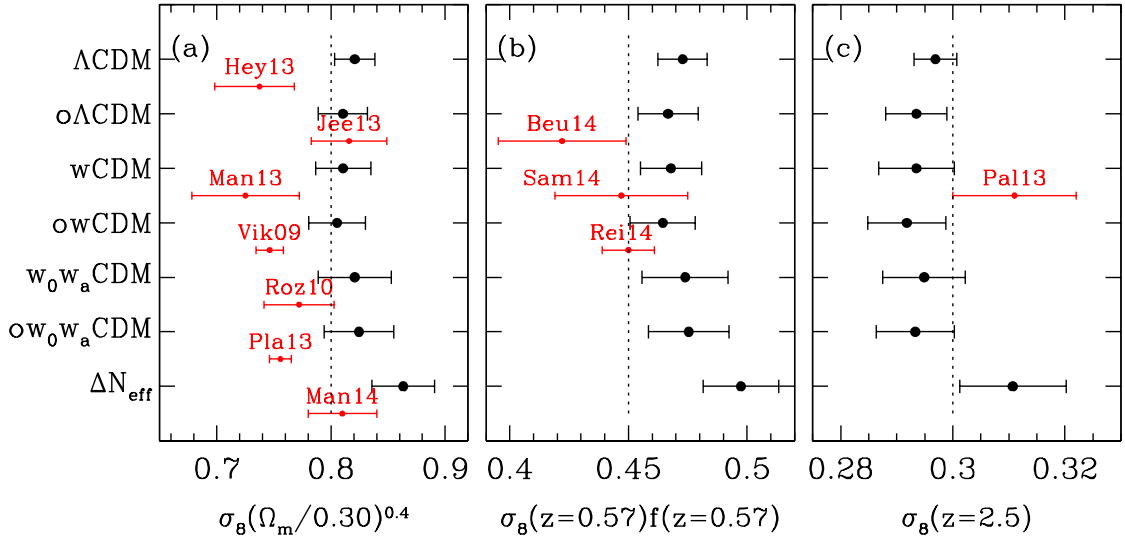

Figure 26.3: Comparison of observational estimates of matter clustering (red points) to the amplitude predicted for a variety of dark energy models constrained by CMB+BAO+SN data (black points) at $z \approx 0$ (left), $z = 0.57$ (middle), and $z = 2.5$ (right), taken from Ref. [28]. Black points with error bars correspond to the 68% confidence range of predictions for the model indicated on the left axis. (Models beginning "o" allow non-zero curvature, while other models assume a flat universe.) Fractional errors for the red points are taken from the observational references given in Ref. [28], and the vertical placement of these points is arbitrary. The observational estimates of $\sigma_8\Omega_m^{0.4}$ in the left panel come from a variety of weak lensing and cluster studies; the estimates of $\sigma_8(z)f(z)$ in the middle panel come from RSD analyses of the BOSS CMASS galaxy sample; and the estimate of $\sigma_8(z = 2.5)$ comes from the 1-dimensional power spectrum of the BOSS Lyman-α forest.

predictions are not a statistical fluctuation in early *Planck* data or a systematic error in the 2013 analysis. (The 2015 *Planck* analysis does change in some significant ways, but the net impact on σ_8 and Ω_m is small.) Second, CMB lensing in *Planck* 2015 yields a roughly 3% measurement of the matter clustering amplitude over an effective redshift range $z \approx 2 - 5$, and this measurement is in excellent agreement with the flat ΛCDM prediction. The CMB lensing and Lyman-α forest measurements imply that deviation from GR-predicted structure growth, if it occurs, must set in mainly at $z < 2$. A low redshift onset would not necessarily be surprising, however, as it would coincide with the era of cosmic acceleration.

26.5. Summary and Outlook

Figure 26.2 and Table 26.2 focus on model parameter constraints, but as a description of the observational situation it is most useful to characterize the precision, redshift range, and systematic uncertainties of the basic expansion and growth measurements. At present, supernova surveys constrain distance ratios at the 1–2% level in redshift bins of width $\Delta z = 0.1$ over the range $0 < z < 0.6$, with larger but still interesting error bars out to $z \approx 1.2$. These measurements are currently limited by systematics tied to photometric calibration, extinction, and reddening, host galaxy correlations, and possible evolution of the SN population. BAO surveys have measured the absolute distance scale (calibrated to the sound horizon r_s) to 4% at $z = 0.15$, 2% at $z = 0.32$ 1% at $z = 0.57$, and 2% at $z = 2.3$. Multiple studies have used clusters of galaxies or weak lensing cosmic shear or galaxy-galaxy lensing to measure a parameter combination $\sigma_8 \Omega_m^\alpha$ with $\alpha \approx 0.3$–0.5. The estimated errors of these studies, including both statistical contributions and identified systematic uncertainties, are about 5%. RSD measurements constrain the combination $f(z)\sigma_8(z)$, with recent determinations spanning the redshift range $0 < z < 0.9$ with typical estimated errors of about 10%. These errors are dominated by statistics, but shrinking them further will require improvements in modeling non-linear effects on small scales. Direct distance-ladder estimates of H_0 now span a small range (using overlapping data but distinct treatments of key steps), with individual studies quoting uncertainties of 3–5%, with similar statistical and systematic contributions. *Planck* data and higher resolution ground-based experiments now measure CMB anisotropy with exquisite precision; for example, CMB measurements now constrain the physical size of the BAO sound horizon to 0.3% and the angular scale of the sound horizon to 0.01%.

A flat ΛCDM model with standard radiation and neutrino content can fit the CMB data and the BAO and SN distance measurements to within their estimated uncertainties, excepting a moderately significant discrepancy for Lyman-α forest BAO at $z = 2.3$. However the CMB+BAO parameters for this model are in approximately 2σ tension with some of the direct H_0 measurements and many but not all of the cluster and weak lensing analyses, disagreeing by about 10% in each case. Agreement of the "inverse distance ladder" value of H_0 with the *Planck*+ΛCDM value suggests that the current direct measurements are systematically high. Alternatively, a change to pre-recombination physics (such as extra relativistic energy density) could shrink the BAO standard ruler and raise the inferred H_0, but changes large enough to allow $H_0 \geq 70\,\mathrm{km\,s^{-1}\,Mpc^{-1}}$ might run afoul of the CMB power spectrum shape. CMB lensing and Lyman-α forest measurements show good agreement with ΛCDM-predicted structure growth at $z \approx 2 - 4$, so if the discrepancies with lower redshift measurements are real then the deviations in growth must set in at late times. At present, none of the tensions in the data provide compelling evidence for new physics. Moving forward, the community will have to balance the requirement of strong evidence for interesting claims (such as $w \neq -1$ or deviations from GR) against the danger of confirmation bias, *i.e.*, discounting observations or error estimates when they do not overlap simple theoretical expectations.

There are many ongoing projects that should lead to improvement in observational constraints in the near-term and over the next 15 years, as summarized above in Table 26.1. Final analyses of *Planck* temperature, polarization, and CMB lensing maps

will improve estimates of the electron scattering optical depth and tighten other parameter constraints, thus sharpening tests based on structure growth. Preliminary results suggest a small reduction in the inferred σ_8, which goes in the direction of reducing tensions. Final analyses of BOSS will slightly reduce BAO errors at $z < 0.6$ and shed light on the significance of the Lyman-α forest tension at $z = 2.3$. Its successor eBOSS will yield the first BAO measurements in the redshift range $1 < z < 2$ and improved precision at lower and higher redshifts. The HETDEX project will measure BAO with Lyman-α emission line galaxies at $z = 2$–3, providing an independent check on Lyman-α forest results with completely different structure tracers. The same galaxy surveys carried out for BAO also provide data for RSD measurements of structure growth and AP measurements of cosmic geometry. With improved theoretical modeling there is potential for substantial precision gains over current constraints from these methods. DES, which started operations in August 2013 and will run through 2018, will provide a sample of several thousand Type Ia SNe, enabling smaller statistical errors and division of the sample into subsets for cross-checking evolutionary effects and other systematics. DES imaging will be similar in depth but 50 times larger in area than CFHTLens, providing a much more powerful weak lensing data set and weak lensing mass calibration of enormous samples of galaxy clusters (tens of thousands). Weak lensing surveys from HSC on the Subaru telescope will be smaller in area but deeper, with a comparable number of lensed galaxies. These new weak lensing data sets hold the promise of providing structure growth constraints at the same (roughly 1%) level of precision as the best current expansion history constraints, allowing a much more comprehensive test of cosmic acceleration models. Controlling measurement and modeling systematics at the level demanded by these surveys' statistical power will be a major challenge, but the payoff in improved precision is large. Uncertainties in direct determinations of H_0 should be reduced by further observations with *HST* and, in the longer run, by Cepheid parallaxes from the *GAIA* mission, by the ability of the *James Webb Space Telescope* to discover Cepheids in more distant SN Ia calibrator galaxies, and by independent estimates from larger samples of maser galaxies and gravitational lensing time delays.

A still more ambitious period begins late in this decade and continues through the 2020s, with experiments that include DESI, Subaru PFS, LSST, and the space missions *Euclid* and *WFIRST*. DESI and PFS both aim for major improvements in the precision of BAO, RSD, and other measurements of galaxy clustering in the redshift range $0.8 < z < 2$, where large comoving volume allows much smaller cosmic variance errors than low redshift surveys like BOSS. LSST will be the ultimate ground-based optical weak lensing experiment, measuring several billion galaxy shapes over 20,000 deg^2 of the southern hemisphere sky, and it will detect and monitor many thousands of SNe per year. *Euclid* and *WFIRST* also have weak lensing as a primary science goal, taking advantage of the high angular resolution and extremely stable image quality achievable from space. Both missions plan large spectroscopic galaxy surveys, which will provide better sampling at high redshifts than DESI or PFS because of the lower infrared sky background above the atmosphere. *WFIRST* is also designed to carry out what should be the ultimate supernova cosmology experiment, with deep, high resolution, near-IR observations and the stable calibration achievable with a space platform.

Performance forecasts necessarily become more uncertain the further ahead we look, but collectively these experiments are likely to achieve 1–2 order of magnitude improvements over the precision of current expansion and growth measurements, while simultaneously extending their redshift range, improving control of systematics, and enabling much tighter cross-checks of results from entirely independent methods. The critical clue to the origin of cosmic acceleration could also come from a surprising direction, such as laboratory or solar system tests that challenge GR, time variation of fundamental "constants," or anomalous behavior of gravity in some astronomical environments. Experimental advances along these multiple axes could confirm today's relatively simple, but frustratingly incomplete, "standard model" of cosmology, or they could force yet another radical revision in our understanding of energy, or gravity, or the spacetime structure of the Universe.

References:

1. A. Einstein, Sitzungsber. Preuss. Akad. Wiss. Berlin (Math. Phys.), 142 (1917).
2. Y.B. Zeldovich, Soviet Physics Uspekhi **11**, 381 (1968).
3. A. Friedmann, On the curvature of space. Z. Phys. **10**, 377 (1922).
4. G. Lemaître, Annales de la Societe Scietifique de Bruxelles **47**, 49 (1927).
5. E. Hubble, Proc. Nat. Acad. Sci. **15**, 168 (1929).
6. A. Einstein and W. de Sitter, Proc. Nat. Acad. Sci. **18**, 213 (1932).
7. For background and definitions, see Big-Bang Cosmology – Sec. 22 of this *Review.*
8. A.G. Riess *et al.* [Supernova Search Team Collab.], Astron. J. **116**, 1009 (1998).
9. S. Perlmutter *et al.*, [Supernova Cosmology Project Collab.], Astrophys. J. **517**, 565 (1999).
10. P. de Bernardis *et al.* [Boomerang Collab.], Nature **404**, 955 (2000).
11. S. Hanany *et al.*, Astrophys. J. **545**, L5 (2000).
12. D.H. Weinberg *et al.*, Phys. Reports **530**, 87 (2013).
13. B. Ratra and P.J.E. Peebles, Phys. Rev. **D37**, 3406 (1988) C. Wetterich, Nucl. Phys. **B302**, 668 (1988).
14. Excellent overviews of the theory and phenomenology of modified gravity models can be found in the review articles of B. Jain and J. Khoury, Ann. Phys. **325**, 1479 (2010) and A. Joyce *et al.*, Phys. Reports **568**, 1 (2015).
15. S.M. Carroll *et al.*, Phys. Rev. **D70**, 043528 (2004).
16. G.R. Dvali, G. Gabadadze, and M. Porrati, Phys. Lett. **B485**, 208 (2000).
17. C.M. Will, Living Reviews in Relativity, **9**, 3 (2006). See also the chapter on Experimental Tests of Gravitational Theory — in this *Review.*
18. B. Jain, V. Vikram, and J. Sakstein, Astrophys. J. **779**, 39 (2013) J. Wang, L. Hui, and J. Khoury, Phys. Rev. Lett. **109**, 241301 (2012).
19. Multiple investigations including M. Fairbairn and A. Goobar, Phys. Lett. **B642**, 432 (2006); Y.-S. Song, I. Sawicki, and W. Hu, Phys. Rev. **D75**, 064003 (2007); C. Blake *et al.*, Mon. Not. Roy. Astron. Soc. **415**, 2876 (2011).
20. E.V. Linder, Phys. Rev. **D72**, 043529 (2005).
21. This is essentially the FoM proposed in the Dark Energy Task Force (DETF) report, A. Albrecht *et al.*, `astro-ph/0609591,` though they based their FoM on the area of the 95% confidence ellipse in the $w_0 - w_a$ plane.

22. For high accuracy, the impact of acoustic oscillations must be computed with a full Boltzmann code, but the simple integral for $r_{\rm s}$ captures the essential physics and the scaling with cosmological parameters.
23. R.A. Sunyaev and Y.B. Zeldovich, Astrophys. Space Sci. **7**, 3 (1970).
24. C. Alcock and B. Paczynski, Nature **281**, 358 (1979).
25. D. Weinberg *et al.*, Snowmass 2013 report on Facilities for Dark Energy Investigations, `arXiv:1309.5380`.
26. B. Jain *et al.*, The Whole is Greater than the Sum of the Parts: Optimizing the Joint Science Return from LSST, Euclid and WFIRST, `arXiv:1501.07897`.
27. W.L. Freedman et al., Astrophys. J. **553**, 47 (2001).
28. E. Aubourg *et al.*, `arXiv:1411.1074` Phys. Rev. D, in press (2015).
29. Planck Collab. 2013 Results XVI, Astron. & Astrophys. **571**, A16 (2014).
30. Planck Collab. 2015 Results I, `arXiv:1502.01582`.
31. Planck Collab. 2015 Results XIV, `arXiv:1502.01590`.
32. Planck Collab. 2015 Results XIII, `arXiv:1502.01589`.
33. M. Betoule *et al.*, Astron. & Astrophys. **568**, 22 (2014).
34. M. Sullivan *et al.*, Astrophys. J. **737**, 102 (2011).
35. J.A. Frieman *et al.*, Astrophys. J. **135**, 338 (2008).
36. N. Suzuki *et al.*, Astrophys. J. **746**, 85 (2012).
37. F. Beutler *et al.*, Mon. Not. Roy. Astron. Soc. **416**, 3017 (2011).
38. A.J. Ross *et al.*, Mon. Not. Roy. Astron. Soc. **449**, 835 (2015).
39. L. Anderson *et al.*, Mon. Not. Roy. Astron. Soc. **441**, 24 (2014).
40. T. Delubac *et al.*, Astron. & Astrophys. **574**, 59 (2015).
41. A.G. Riess *et al.*, Astrophys. J. **730**, 119 (2011).
42. W.L. Freedman *et al.*, Astrophys. J. **758**, 24 (2012).
43. G. Efstathiou, Mon. Not. Roy. Astron. Soc. **440**, 1138 (2014).
44. M. Rigault *et al.*, Astrophys. J. **802**, 20 (2015).